

On the Coupling of Flow and Elastic Expansion of Porous Media

Arnold Bachrach & Yaniv Edery

Faculty of Civil and Environmental Engineering, Technion, Haifa, Israel.

Abstract

Pressurized fluid injection into underground rocks occurs in applications like hydraulic fracturing, wastewater disposal, and carbon sequestration, and may lead to human-induced earthquakes and surface uplift. The fluid injection raises the pore pressure within the porous rocks, while deforming them, yet this coupling is not fully validated for risk assessment as experimental studies of rocks are usually limited to postmortem inspection and cannot capture the complete deformation process in time and space. We investigate injection-induced elastic expansion of a unique rock-like medium mimicking the deformation of sandstone and show that pressurized flow through porous medium will result in a non-uniform expansion following the local pore pressure changes. We fully model this coupling using the theory of poroelasticity. As our porous medium has the same deformation scale as real rock, making our conclusions applicable for injection induced expansion of the underground.

Introduction

In recent years the coupling of flow, pressure and deformation in porous media proves to be seminal to our understanding of fluid injections into the underground, as is the case for hydraulic fracturing¹, enhanced geothermal energy production², wastewater disposal³⁻⁵, and carbon sequestration^{6,7}. The fluid injection raises the pore pressure within the underground rocks, leading to human-induced earthquakes^{3-5,8} and surface uplift^{3,5,9}. While human-induced earthquakes are attributed to fault reactivation⁸, surface uplift is a phenomenon that can be attributed to elastic expansion of the underground rocks^{3,10,11}. Moreover, the elastic response of the medium to fluid injection can induce underground stresses and facilitate fault reactivation^{12,13}. Early observations on the coupling of flow, pore-pressure, and elasticity has been documented by King (1892)¹⁴, as he measured water-level fluctuations in wells due to

passing trains^{14,15}. It was later shown by Jacob (1939)¹⁵ that the weight of a train can elastically compresses the underground aquifer, hence raising its pore water pressure and elevating the surrounding wells water-level. These observations were accompanied by comprehensive scientific study, mainly in the context of soil consolidation^{16–18} and elastic storage in a confined aquifer^{19–21}, formulating the theory of *Poroelasticity*.

Originally, the poroelastic theory was developed for the case of fluid outflow from the porous medium- weather by fluid extraction^{19,21} or by loading^{16,17}, hence, experiments are needed to prove and demonstrate its applicability in fluid injection scenarios. Yet, injection experiments on rocks are usually limited to postmortem inspection^{22,23} and cannot capture the complete spatial and temporal dynamics of the deformation process. Although experiments on soft or loosely consolidated materials provide insights on injection induced deformation^{24–26}, the materials used in these experiments are often very different from real rocks by their internal structure, mechanical behavior, and permeability.

In this study, we will investigate injection-induced poroelastic expansion of a unique rock-like medium that mimics the deformation of sandstone under low pressure. Our medium undergoes all the deformation range of real rock, from elastic to plastic, while allowing us to capture the whole internal displacement field. We will show that the mechanism behind steady-state fluid injection leads to non-uniform expansion of the medium, a phenomenon that we fully model using the theory of poroelasticity^{16–18,27}.

Methods

To investigate the coupling of pressurized flow with elastic deformation, we developed a transparent artificial rock by sintering PMMA (Polymethyl Methacrylate) beads with a mean diameter of 78 microns (see Appendix A, figure 4 for details on the grain size distribution). We chemically sinter the sample inside a PMMA chamber using an Acetone mixture that dissolves the edges of the beads and subsequently drains the mixture, allowing the beads to solidify together into a rock-like porous material (figure 1a, 1b). At the injection point, the sample is fixed by an epoxy glue to the flow-cell wall while the outlet edge remains free (figure 1a). The artificial rock porosity ($n = 0.43$) is measured from micro-CT scan of the sample (Appendix A,

figure 5). Using the Kozeny-Carman equation^{28,29}, we calculate the permeability ($k = 5.85 \times 10^{-12} \text{ m}^2$) and show that it corresponds to a high-permeability sandstone³⁰. To track the local deformation, we incorporate and solidify 1.2% fluorescent Polyethylene microspheres (106-125 microns in diameter) within the sample (figure 1b). The tracking is achieved by saturating the sample with oil (Cargille immersion liquid) that has a matching refractive index as the PMMA (RI=1.49), transforming the sample from opaque to transparent, apart from the fluorescing microspheres which are excited by 460 nm LED light and emit at a range of 580-700 nm, which is filtered by a long-pass 625 nm filter (figure 1c).

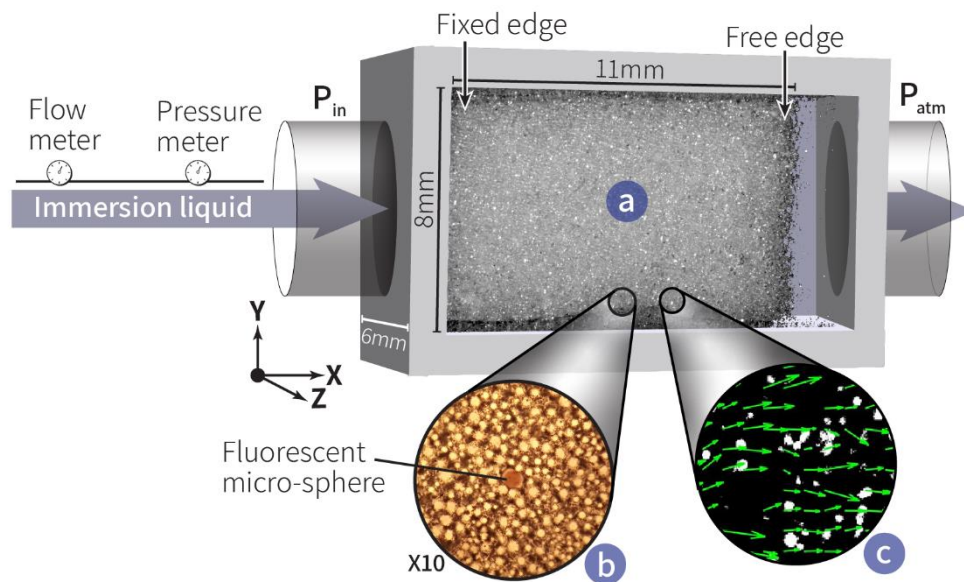


Figure 1. Experimental set-up. a: The artificial rock-like sample within the flow-cell, where the injection point is fixed to the flow-cell wall while the outlet edge remains free. b: The sintered PMMA beads with the fluorescent micro-spheres forming the artificial rock, as seen under optical microscope. c: Tracking and analysis of the filtered fluorescent microspheres by an ultra-high-speed camera and PIV software³¹, respectively, which provide the whole displacement field within the sample.

The oil flow through the artificial rock is driven by a pressure difference using a pressure pump (Fluigent-LU-FEZ-7000) as we monitor the inlet pressure and fluid discharge by a pressure-sensor (Fluigent-EIPS7000) and flowmeter (Fluigent-FLU-XL), respectively. This pressure difference increases by 70 mbar/sec as we track the deformation by the fluorescent microspheres movement using a high-resolution (4Mpx) ultra-high-speed camera (Phantom-v2640) at a rate of

100 frames per second at 12 bits. A Particle Image Velocimetry (PIV) software (PIVlab 2.50)³¹ provides the whole displacement field within the sample for each timestep by analyzing the fluorescent microsphere's joint movement (figure 1c, Appendix B, figure 6). We calculated the PIV accuracy as 0.57 microns (0.04 pixels) by applying the analysis on the system without any pressure difference, where the displacement of the fluorescent beads is zero, to measure the imaging noise.

Results

The embedded fluorescent micro-sphere movement in the artificial rock allows us to calculate the extension of the sample using the PIV software³¹ for each inlet pressure that drives the flow, thus, providing a pseudo-stress-strain curve as in a pulling test^{32,33} (figure 2a). In figure 2a, the x axis is the sample's total extension, measured from the free edge displacement (figure 1a), averaged over the y axis of the sample, and normalized by the sample's initial length. Thus, providing the overall strain of the sample. The y axis in figure 2a is the inlet pressure, representing the stress in the pseudo-stress-strain curve. Looking at the curve, we identify a trend similar to that of a pulled rock in a tensile test: a linear elastic chapter for pressures of up to 0.084 MPa, followed by a non-linear elasto-plastic chapter. Moreover, the normalized extension magnitude of our sample is on the same scale as a pulled sandstone strain in a tensile test (figure 2b)³². We verify the pseudo-stress-strain curve transition from elastic to plastic by a cyclic pressure test (figure 2c), where we apply cycles of pressure increase followed by a pressure decrease, with an increasingly higher pressure for each cycle. As seen in figure 2c, the strain at cycle 1, reaching about 0.1 MPa, is completely reversible, meaning that the deformation is elastic. However, in the following cycles, we can see a larger and larger remnant strain, manifested in the hysteresis of the cycle, meaning that indeed a plastic component is added to the deformation.

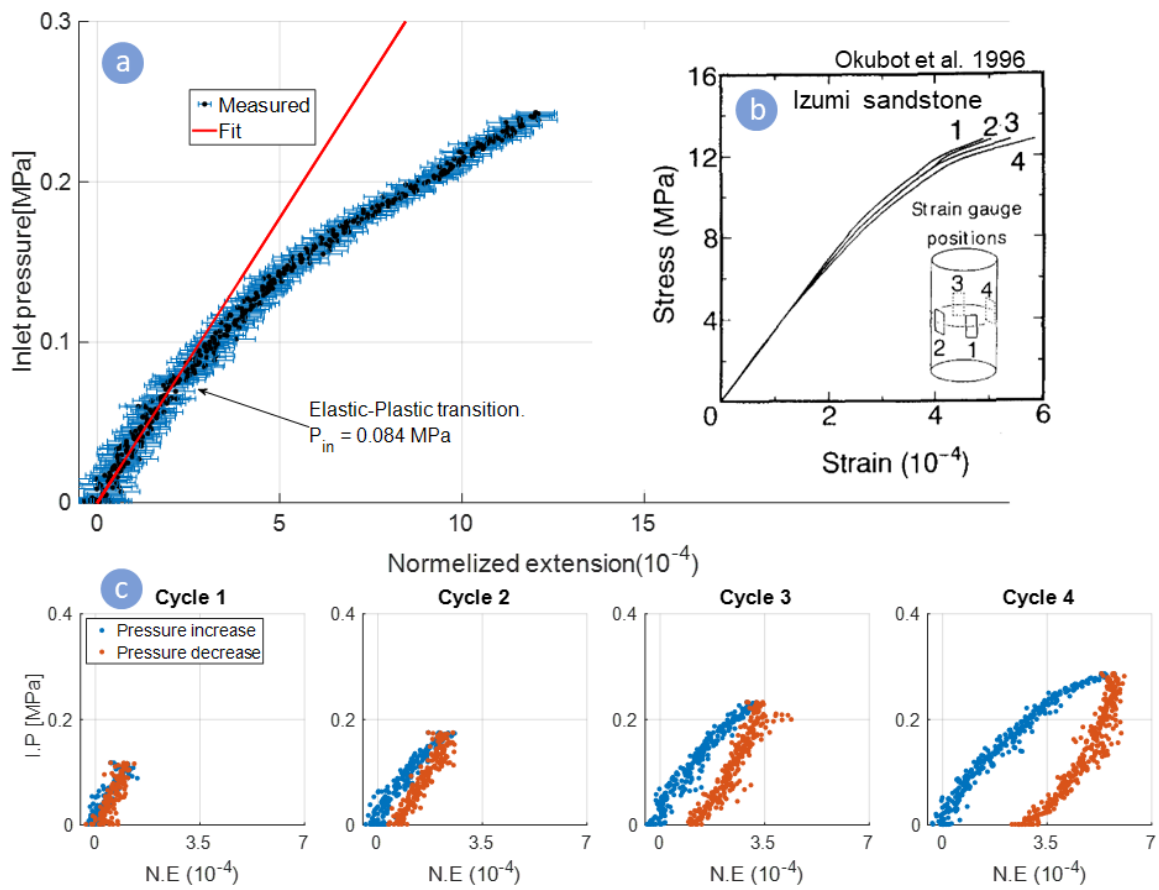


Figure 2. Pseudo stress-strain curves. a: The strain is the total extension normalized by the sample's initial length, and the stress is the measured inlet pressure. The curve follows the same transition between elastic to plastic deformation observed in a pulled rock. The error of the pressure sensor ($1.6e-3$ to $4e-3$ MPa) is negligible compared to the PIV error (0.6 microns). b: Comparison of our results to a sandstone pulling test done by Okubot et. al (1996)³². The extension of our sample is similar not only in the general trend but also in the scale of strain. c: Cyclic pressure tests, where the end pressure applied on the sample is increasing on every cycle, and subsequently decrease. The strain at cycle 1 reaches about 0.1 MPa is completely reversible, indicating an elastic response, however, the following cycles with higher end pressure are not reversible, showing a remnant plastic strain manifested by each cycle hysteresis. I.P: inlet pressure, N.E: normalized extension.

Our artificial rock simulates real rock deformation by moving from the elastic to the elastoplastic regime. However, unlike opaque rocks, it allows us to quantify the coupling between the pressurized flow and the deformation by analyzing the internal local displacement as the pressure drops from inlet to outlet. We analyze the internal displacement of the experiment in figure 2a by calculating the mean displacement over the sample's y axis for each 224 microns along x (see more details in Appendix B). Figure 3 shows the measured displacement along the sample for three different inlet pressures from the same experiment. As can be seen, the increase in displacement along x is not distinctly linear as one would expect from the analogy to a tensile test, suggesting a non-uniform strain distribution.

To understand the measured results, we developed an analytical model for the system based on Hooke's law, Darcy's law, and Terzaghi's concept of effective stress^{17,18,34}, which coincide with Biot's theory of poroelasticity¹⁶ for incompressible fluid and grains.

The *pore Reynolds number* along the experiment has been calculated to be <0.1 , hence the flow through the porous medium should be governed by Darcy's law^{29,35}, where gravitational forces and momentum are negligible compared to the pressure difference. Our boundary conditions allow flow just in the x direction, hence we can use the one-dimensional Darcy's law that linearly relates the fluid flux (q) with the pore pressure drop ($\frac{dp}{dx}$) by the permeability (k) and the dynamic viscosity of the fluid ($\mu = 11.7 \text{ mPa} \cdot \text{s}$).

$$q = -\frac{k}{\mu} \left(\frac{dp}{dx} \right)$$

1

Due to the small elastic deformations of the artificial rock (figure 2a), the change in porosity measured from the sample's elongation is negligible ($\Delta n < 0.1\%$), hence we will treat the permeability as a constant. We further assume that the response time for each inlet pressure is instantaneous due to the small sample size, so for each inlet pressure the system is at steady state and the flux is constant along the sample ($\frac{dq}{dx} = 0$), providing the Laplace's equation for the pore-pressure ($\frac{d^2p}{dx^2} = 0$). Under the condition that $p(x = 0) = p_{injection}$ and $p(x = L) = p_{atm}$ for a sample at length L , the pore pressure along the sample can be derived:

$$p(x) = -\frac{p_{in}}{L}x + p_{in}$$

2

Although the sample is extending like in a tensile test (figure 2), the boundary conditions are that of Oedometric test^{36,37}, where the sample is compressed vertically while confined laterally. This is due to the tensional stress caused by pore pressure in all directions^{16–18,34}. Hence, our set-up

allows the sample to expand only in the x direction, while both y and z directions are constrained by the flow-cell walls (see figure 1 for orientation). That is, there is one direction of stress (σ_x) and free strain (e_x) and two other directions of no strain ($e_y = e_z = 0$) and reaction stresses (σ_y, σ_z), just like in Oedometric test. Using these boundary conditions with Hook's law for isotropic elastic body, while addressing the presence of fluid through Terzaghi's concept of effective stress^{17,18,34} leads to the following relation (see Appendix C for derivation):

$$e_x = \frac{1}{E_{oed}} p$$

3

Where E_{oed} is the Oedometric modulus^{36,37}. Substituting equation (2) in (3) gives:

$$e_x = \frac{du}{dx} = \frac{1}{E_{oed}} p_{in} \left(1 - \frac{x}{L}\right)$$

4

Where u is the displacement in the x direction.

Under the condition that the inlet boundary is fixed ($u(x = 0) = 0$), we integrate (4) to derive a solution for the displacement at each location along the x axis:

$$u(x) = -\frac{p_{in}}{2E_{oed}L} x^2 + \frac{p_{in}}{E_{oed}} x$$

5

applying equation (5) on the sample's edge ($x = L$) we can write:

~ 7 ~

$$p_{in} = 2E_{oed} \frac{u_{edge}}{L}$$

6

Equation (6) suggests that when the one-dimensional strain (u_{edge}/L) is caused by flow instead of external force, the sample's edge will displace as if the material is twice as stiffer than in a regular Oedometric test. This is due to the fact that in regular Oedometric test the stress is constant along the medium, while here the effective stress follows the pore pressure and hence decreases along the sample. Moreover, $2E_{oed}$ is exactly the slope of our pseudo stress-strain curve (figure 2a, red line). Hence, from the slope of the measured pseudo stress-strain curve we can calculate E_{oed} , and use equation (5) to model the displacement in each point along our sample for all the inlet pressures and *without any fitting parameters* (figure 3, brown line). As can be seen in figure 3, the model agrees extremely well with the measured data. Knowing the value of E_{oed} , equation (3) can be used for calculating the strain along the sample (figure 3, purple line). Following the pore pressure, the strain decreases linearly along the sample. While the injection area is highly expanding, the outlet area hardly strains.

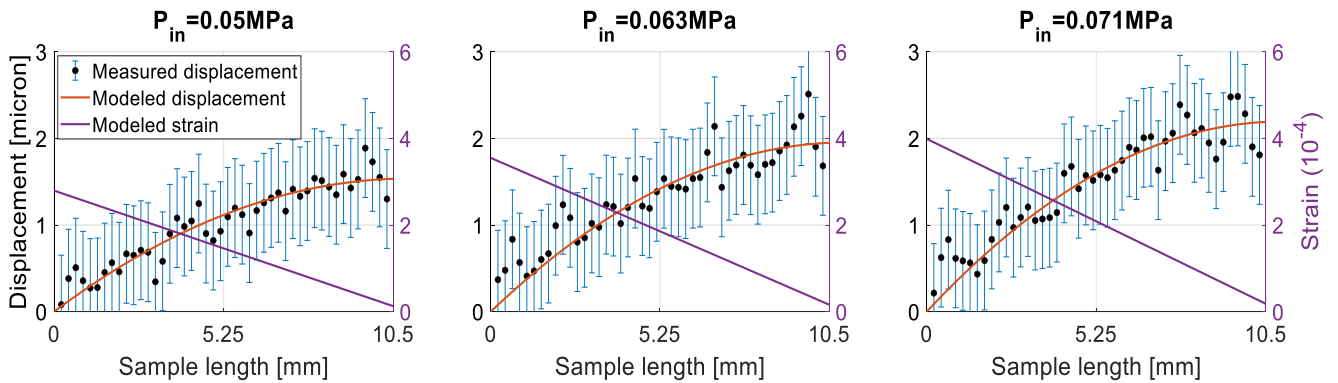


Figure 3. Internal displacement along the sample. The model we derived based on the theory of poroelasticity (brown curve) predicts accurately the measured displacement (black dots), without any fitting parameters. Using the model we also calculated the internal strain (purple curve), which decreases linearly along the medium, following the pore pressure.

Discussion

This study confirms and describes the applicability of the poroelastic theory in modeling injection induced expansion of porous media. We use a unique rock-like medium together with a novel experimental system to visualize the internal displacement field induced by pressurized flow through the medium. As the artificial rock has the same deformation scale as real rock, our results are valid for predicting poroelastic expansion in the underground. We found that one-dimensional pressurized flow through porous medium induces linear decreasing expansion, which lead to parabolic increase in the cumulative displacement along the medium, a phenomenon that we modeled accurately without any fitting parameters using Terzaghi's concept of effective stress^{17,18}.

Parker (1987)²⁴ , following Biot (1941)¹⁶, mentioned the same pressure-strain relation we expressed here in equation (4), while studying injection induced compaction of polyurethane foam. However, this relation was not validated nor related to measured data, as the foam used showed a strong and complex dependence of permeability and stiffness in strain. We interpreted the boundary conditions of the presented experiment as that of Oedometric test ^{36,37}, and we further suggest that this boundary conditions are also appropriate for the underground conditions, where there is one direction of free displacement (the surface) and two other directions of limited displacement (the subsurface). Hence the Oedometric modulus might be suitable for modeling the stiffness of the underground rocks in fluid injection scenarios. Moreover, the analytical model together with the experimental results we presented here suggests a non-uniform expansion of the fluid injected reservoir, possibly affecting the structure and range of surface uplift. Although this work was focused on elastic deformation, our rock-like medium has the potential to explore the full range of elasto-plastic transition, which we will investigate in a subsequent study.

Acknowledgments

We thank Alberto Guadagnini and Gabriele Dellavecchia for their insightful comments and discussions. We also thank Ludmila Abezgauz, Shaimaa Sulieman and Martin Stolar for their help in the experiments. A.B. acknowledge The Nancy and Stephen Grand Technion Energy

Program (GTEP) for supporting this research. Y.E. and A.B. thank the support of ISF-NSFC (grant No. 3333/19)

Reference

1. Bao, X. & Eaton, D. W. INDUCED SEISMICITY Fault activation by hydraulic fracturing in western Canada. (2016).
2. Deichmann, N. & Giardini, D. Earthquakes Induced by the Stimulation of an Enhanced Geothermal System below Basel (Switzerland). *Seismological Research Letters* **80**, 784–798 (2009).
3. Manoochehr Shirzaei, William L. Ellsworth, Kristy F. Tiampo, Pablo J. González & Michael Manga. Surface uplift and time-dependent seismic hazard due to fluid injection in eastern Texas. *Science (1979)* (2016) doi:10.1126/science.aah3398.
4. Horton, S. Disposal of hydrofracking waste fluid by injection into subsurface aquifers triggers earthquake swarm in central arkansas with potential for damaging earthquake. *Seismological Research Letters* **83**, 250–260 (2012).
5. Juncu, D. *et al.* Injection-induced surface deformation and seismicity at the Hellisheidi geothermal field, Iceland. *Journal of Volcanology and Geothermal Research* **391**, (2020).
6. Snæbjörnsdóttir, S. *et al.* Carbon dioxide storage through mineral carbonation. *Nature Reviews Earth and Environment* vol. 1 90–102 Preprint at <https://doi.org/10.1038/s43017-019-0011-8> (2020).
7. Zoback, M. D. & Gorelick, S. M. Earthquake triggering and large-scale geologic storage of carbon dioxide. *Proceedings of the National Academy of Sciences of the United States of America* vol. 109 10164–10168 Preprint at <https://doi.org/10.1073/pnas.1202473109> (2012).
8. Ellsworth, W. L. *Injection-Induced Earthquakes*. <https://www.science.org> (2013).
9. Onuma, T. & Ohkawa, S. Detection of surface deformation related with CO₂ injection by DInSAR at In Salah, Algeria. in *Energy Procedia* vol. 1 2177–2184 (2009).
10. Chen, Z. R. Poroelastic model for induced stresses and deformations in hydrocarbon and geothermal reservoirs. *J Pet Sci Eng* **80**, 41–52 (2011).
11. Palmer, I. D. Uplifts and Tilts at Earth's Surface Induced by Pressure Transients From Hydraulic Fractures. *SPE Production Engineering* **5**, 324–332 (1990).
12. Chang, K. W. & Segall, P. Injection-induced seismicity on basement faults including poroelastic stressing. *J Geophys Res Solid Earth* **121**, 2708–2726 (2016).
13. Segall, P. & Lu, S. Injection-induced seismicity: Poroelastic and earthquake nucleation effects. *J Geophys Res Solid Earth* **120**, 5082–5103 (2015).
14. King, F. *Observations and Experiments on the Fluctuations in the Level and Rate of Movement of Ground-water on the Wisconsin Agricultural Experiment Station Farm*. (1892).
15. Jacob C. E. FLUCTUATIONS IN ARTESIAN PRESSURE PRODUCED BY PASSING RAILROAD-TRAINS AS SHOWN IN A WELL ON LONG ISLAND, NEW YORK. (1939).

16. Biot, M. A. General theory of three-dimensional consolidation. *J Appl Phys* **12**, 155–164 (1941).
17. Terzaghi. Die Berechnung der Durchlässigkeit des Tones aus dem Verlauf der hydromechanischen Spannungserscheinungen. *Sitzungsber. Akad. Wiss.(Wien). Math.-Naturwiss.* (1923).
18. Terzaghi. *Theoretical Soil Mechanics*. John Wiley & Sons (John Wiley & Sons, Inc, 1943).
19. C. E. Jacob. *Geology and water resources of south-central Nebraska*. U. S. Geol. Surv. W.-S. Paper vol. 779 (1940).
20. Meinzer, O. E. Compressibility and elasticity of artesian aquifers. *Economic Geology* **23**, 263–291 (1928).
21. Theis, C. v. The significance and nature of the cone of depression in ground-water bodies. *Economic Geology* **33**, 889–902 (1938).
22. King, M. *et al.* *Mechanics of Hydraulic Fracturing*. <http://onepetro.org/trans/article-pdf/210/01/153/2176767/spe-686-g.pdf> (1956).
23. Bohlooli, B. & de Pater, C. J. Experimental study on hydraulic fracturing of soft rocks: Influence of fluid rheology and confining stress. *J Pet Sci Eng* **53**, 1–12 (2006).
24. Parker, K. H., Mehta, R. v & Caro, C. G. *Steady Flow in Porous, Elastically Deformable Materials*. http://asmedigitalcollection.asme.org/appliedmechanics/article-pdf/54/4/794/5459498/794_1.pdf (1987).
25. Hewitt, D. R., Nijjer, J. S., Worster, M. G. & Neufeld, J. A. Flow-induced compaction of a deformable porous medium. *Phys Rev E* **93**, (2016).
26. MacMinn, C. W., Dufresne, E. R. & Wettlaufer, J. S. Fluid-driven deformation of a soft granular material. *Phys Rev X* **5**, (2015).
27. Herbert F. Wang. *Theory of Linear Poroelasticity with Applications to Geomechanics and Hydrogeology*. (Princeton university press, 2017).
28. Freeze & Cherry. *GROUNDWATER*. (Prentice Hall, Inc, 1979).
29. Bear, J. & York, N. *dynamics of fluids in porous media*. (DOVER PUBLICATIONS, INC, 1972).
30. Jaeger, Cook & Zimmerman. *Fundamentals of Rock Mechanics*. (Blackwell, 2007).
31. Thielicke, W. & Sonntag, R. Particle Image Velocimetry for MATLAB: Accuracy and enhanced algorithms in PIVlab. *J Open Res Softw* **9**, 1–14 (2021).
32. Okubot, S. & Fukuit, K. *Complete Stress-Strain Curves Rock Types in Uniaxial Tension for Various*. *J. Rock Mech. Mht. Sci. & Geomech. Abstr* vol. 33 (1996).
33. Stoxreiter, T., Gehwolf, P. & Galler, R. Alternative Approaches for the Determination of Unconfined Rock Deformation and Strength Properties. *Rock Mech Rock Eng* **53**, 411–433 (2020).
34. Nur, A. & Byerlee, J. D. An exact effective stress law for elastic deformation of rock with fluids. *J Geophys Res* **76**, 6414–6419 (1971).

35. Sobieski, W. & Trykozko, A. *DARCY'S AND FORCHHEIMER'S LAWS IN PRACTICE. PART 1. THE EXPERIMENT. Technical Sciences* vol. 17 (2014).
36. Selvadurai, A. *Elastic analysis of soil-foundation interaction*. (2013).
37. Sawicki, A. & Swidzinski, W. *ELSEVIER Elastic moduli of non-cohesive particulate materials. POWDER TECHNOLOGY* vol. 96 (1998).
38. systems, N. O.-I. transactions on, man, undefined, cybernetics, and & 1979, undefined. A threshold selection method from gray-level histograms. *cw.fel.cvut.cz*.
39. Thielicke, W. & Sonntag, R. Particle Image Velocimetry for MATLAB: Accuracy and enhanced algorithms in PIVlab. *J Open Res Softw* **9**, 1–14 (2021).

Appendix A: Material properties

The grain size distribution of the porous medium used in this research (figure 4) was derived for the unconsolidated PMMA particles composing the medium by a Dynamic light scattering analysis (DLS). The mean grain size of the medium is 78 microns. The fluorescent beads (106-125 microns in diameter) are within the range of the initial distribution and fit within the tail of it.

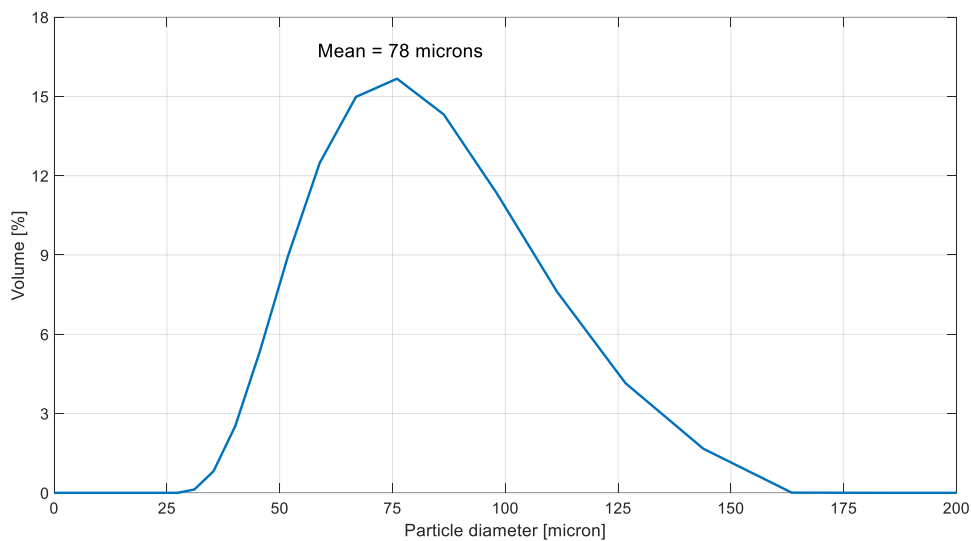


Figure 4. The artificial rock grain distribution, achieved through DLS analysis on the non-sintered PMMA beads.

The sintered porous medium has been scanned by micro-CT to study its internal structure (figure 5a, b). For calculating the porosity, the whole scanned volume (figure 5b) has been binarized through Matlab, using Otsu's method³⁸ and the porosity ($n = 0.43$) has been calculated as the ratio between the black pixels (voids) to the overall number of pixels in the volume. The big black circles in figure 5b are voids created due to trapped air bubbles at the sintering process. These air bubbles are released from the medium as we saturate the sample with oil at the start of the injection experiment.

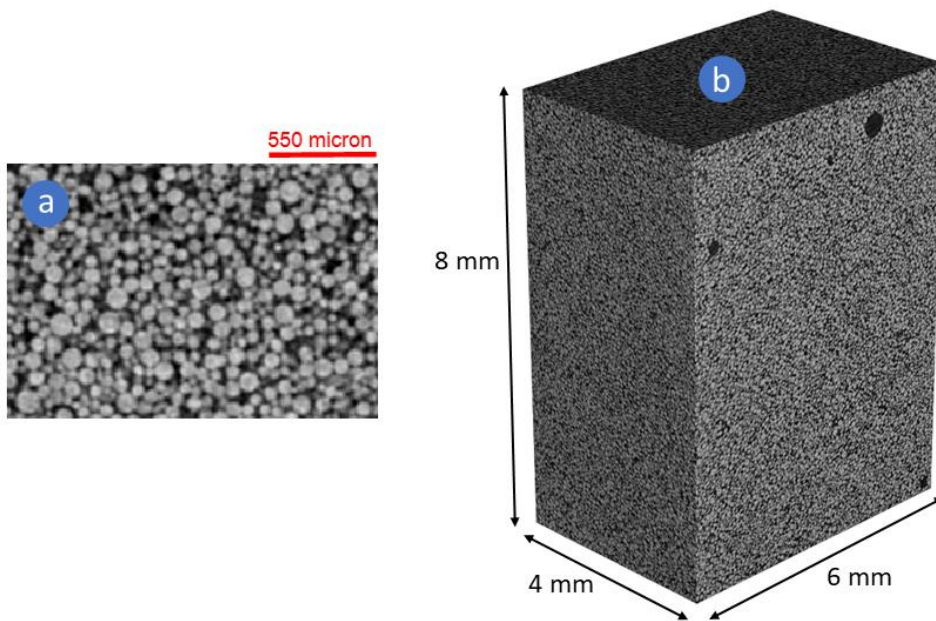


Figure 5. Micro CT scan of the artificial rock. a: One internal plane (cropped). b: The whole scanned volume. The big black circles are voids created due to trapped air bubbles in the sintering process.

The porosity analysis has been verified in another test in which the consolidated porous medium is saturated with oil inside the flow cell. The weight of the oil reservoir is measured before the saturation and after it so the difference is exactly the weight of the oil inside the porous medium. Knowing the density of the oil, the pore fluid volume is calculated and divided by the measured volume of the medium to achieve the porosity. The porosity value that was calculated from this test was 0.42, almost the same as the porosity value from the CT test.

Appendix B: PIVlab Analysis

The PIV calculates the mean displacement value for each 448X448 microns (32X32 pixels) along the sample (figure 6). This size of interrogation area was optimized by the software³⁹, with 224 microns (16 pixels) overlap between each area. We analyze the internal displacement of the experiment in figure 2a by calculating the mean displacement of each column of interrogation units along the sample's x axis. The mean displacement is correlated to the distance of the

interrogation unit center from the sample's inlet, resulting in internal displacement values for each 224 microns along the sample (figure 3).

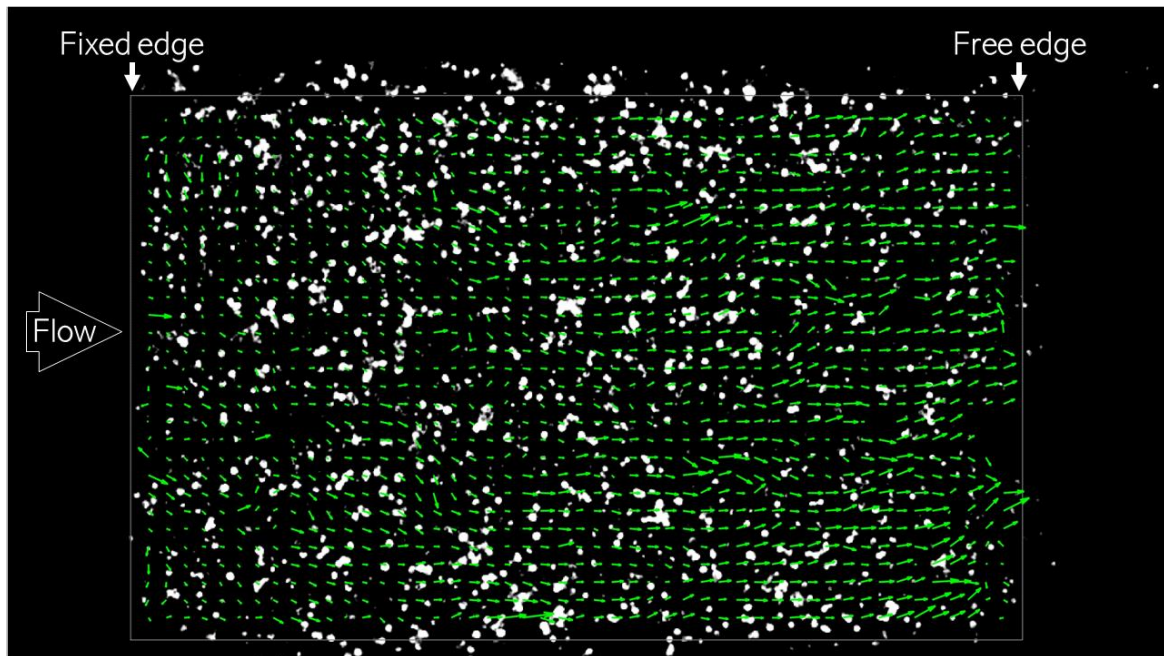


Figure 6. Full PIVlab analysis³⁹. The PIV analysis provides the whole internal displacement field of the sample for each pressure difference applied.

Appendix C: Model derivation

The stress (σ) - strain (e) relations are governed by Hooke's law for an isotropic elastic body:

$$e_x = \frac{\sigma_x}{E} - \frac{\nu}{E}(\sigma_y + \sigma_z)$$

1

$$e_y = \frac{\sigma_y}{E} - \frac{\nu}{E}(\sigma_x + \sigma_z)$$

2

$$e_z = \frac{\sigma_z}{E} - \frac{\nu}{E}(\sigma_y + \sigma_x)$$

3

Where E is Young's modulus, and ν is Poisson's ratio.

To account for the presence of fluid in the medium, we will use Terzaghi's concept of effective stress^{17,18,34}, which coincides with Biot's theory of poroelasticity¹⁶ for incompressible grains and fluid. Defining tension and expansion as positive:

$$\sigma' = \sigma_{ex} + p$$

4

where σ' is the effective stress, σ_{ex} is external stress and p is the pore-pressure.

For this set-up, there is no external stress in the x direction, thus:

$$\sigma'_x = p$$

5

Our boundary conditions dictate that $e_y = e_z = 0$, therefore, equation (2) in terms of effective stress can be written as:

$$0 = \frac{\sigma'_y}{E} - \frac{\nu}{E}(\sigma'_x + \sigma'_z)$$

6

Assuming that $\sigma'_y = \sigma'_z$ we can write:

$$0 = \frac{\sigma'_y}{E} - \frac{\nu}{E}(\sigma'_x + \sigma'_y)$$

7

Using equation (7), we can find σ'_y as function of σ'_x :

$$\sigma'_y = \frac{\nu}{1 - \nu} \sigma'_x$$

8

Substitution of equation (8) in (1) gives:

$$e_x = \frac{\sigma'_x}{E} - \frac{\nu}{E} \left(2 \frac{\nu}{1 - \nu} \sigma'_x \right)$$

9

Equation (9) can be rewritten as:

$$e_x = \frac{1}{E} \left(1 - \frac{2\nu^2}{1 - \nu} \right) \sigma'_x$$

10

Substituting equation (5) in (10) gives:

$$e_x = \frac{1}{E} \left(1 - \frac{2\nu^2}{1-\nu} \right) p$$

11

The coefficient of the pore-pressure is essentially the inverse of the *Oedometric modulus*^{36,37}.

That is:

$$e_x = \frac{1}{E_{oed}} p$$

12

Where:

$$E_{oed} = \frac{E}{1 - \frac{2\nu^2}{1-\nu}}$$

13